# Morphology of Anion-Conducting Ionenes Investigated by X-ray Scattering and Simulation

Eric M. Schibli,[†] Andrew G. Wright,[‡] Steven Holdcroft,[‡] and Barbara J. Frisken*,[†]

[†]Department of Physics and [‡]Department of Chemistry, Simon Fraser University, Burnaby, BC, Canada V5A 1S6

S *Supporting Information*

ABSTRACT: We have studied the morphology of a novel series of benzimidazole-based ionenes, methylated poly-(hexamethyl-*p*-terphenylbenzimidazolium) (HMT-PMBI), in halide form. Materials with anion-exchange capacities ranging from 0 to 2.5 mequiv/g were studied. X-ray scattering reveals three length scales in the materials: ion−polymer spacing (4 Å), polymer−polymer interchain spacing (6 Å), and an intrachain repeat distance (20 Å). No long-range structure is apparent above the monomer length, which is rare in ion-conducting polymer membranes. In preliminary molecular dynamics simulations, water molecules were observed forming chains between ions, even at a modest level of hydration, providing an interpenetrating network where conductivity can occur.
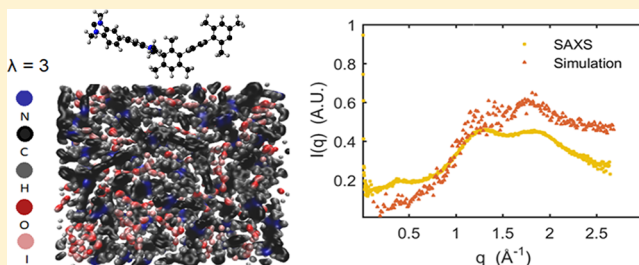
INTRODUCTION

Anion-exchange membranes (AEMs), formed from synthetic macromolecules containing fixed cationic sites and dissociated anions, are currently of considerable interest because of their importance in electrochemical technologies such as fuel cells, electrolysis,[1] wastewater treatment,[2] redox-flow batteries,[3] biofuel cells,[4] and desalination.[5] In particular, hydroxide ion AEM fuel cells (AEMFC) and electrolyzers are energy converters of emerging interest because the use of non-precious-metal catalysts in alkaline media offers an advantage over devices based on proton-exchange membranes.[6] However, challenges to widespread adoption of AEMs for these technologies include poor stability of polymeric materials in basic media[7] and comparatively poor ion conductivity due to the low diffusion coefficient of the hydroxide ion and its carbonation when exposed to air. The past 5 years have shown significant increases in reported AEMFC peak power and current densities; however, membrane stability remains a significant concern.[8] To address this, numerous cationic moieties have been investigated for hydroxide stability, including guanidinium-,[9] DABCO-,[10] imidazolium-,[11] pyrrolidinium-,[12] sulfonium-,[13] phosphonium-,[14] and ruthenium-based cations.[15]

This work focuses on a material that is based on a sterically protected benzimidazolium-based cation, methylated poly-(hexamethyl-*p*-terphenylbenzimidazolium) (HMT-PMBI). This material has a tunable ion-exchange capacity and has been proven to possess significant ion conductivity and exceptional hydroxide stability.[16,17] HMT-PMBI has been demonstrated in both fuel cells and water electrolyzers.[17] In fuel-cell testing, HMT-PMBI cells exhibited exceptional stability leading to longer lifetimes. HMT-PMBI falls under a class of polymers known as ionenes for which the cation is an

integral feature of the polymer backbone. In the case of HMT-PMBI, the stability of the cation is provided via steric protection by methyl groups;[18] however, no investigations of the morphology or conduction mechanisms for HMT-PMBI or similar polymers have been reported to date.

An understanding of polymer morphology is an important component in the design of improved materials for polymer−electrolyte membranes.[19] Ion conduction involves the diffusion of ions through water-rich domains and depends both on charge content of the hydrophilic domains and on their interconnectivity. The morphology also impacts chemical and mechanical stabilities.

In this paper, we report a detailed analysis of the morphology of HMT-PMBI. We performed small- and wide-angle X-ray scattering (SAXS and WAXS) on two halide forms of HMT-PMBI—HMT-PMBI(I⁻) and HMT-PMBI(Cl⁻)—in various conditions: in a vacuum, in ambient conditions, after soaking in water, and after stretching. We also performed density functional theory calculations and preliminary molecular dynamics calculations to aid interpretation of our results.

MATERIALS AND METHODS

HMT-PMBI is a polymer composed of up to three submolecular units, *x*, *y*, and *z*, with each unit contributing either +0, +1, or +2 to the total charge of the backbone; the chemical structures are shown in Figures 1a, 1b, and 1c, respectively. The cationic benzimidazolium units are separated by a series of neutral aromatic rings to reduce the material's solubility. The ion-exchange capacity (charge content along the
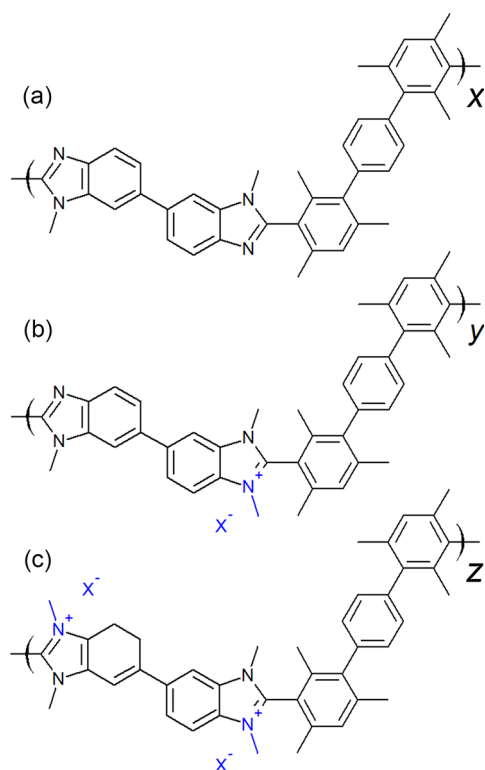
Figure 1. Chemical structure of HMT-PMBI, a polymer composed of three submolecular units: *x*, *y*, and *z*, as shown in (a), (b), and (c), respectively. The anion, X⁻, is iodide immediately following synthesis.

Table 1. Properties of HMT-PMBI at Varying Degrees of Methylation (dm)

dm (%)	anion[a]	IEC (mequiv/g)	water uptake (wt %)	σ^b (mS/cm)
65.9	HCO_3^-/CO_3^{2-}	1.1	29 ± 4	0.10 ± 0.03
80.2	HCO_3^-/CO_3^{2-}	2.0	42 ± 3	1.4 ± 0.2
89.7	HCO_3^-/CO_3^{2-}	2.5	54 ± 2	10.0 ± 1.2
97.5	HCO_3^-/CO_3^{2-}	3.1	NA[c]	NA[c]
80.2	Cl^-	1.8	24 ± 8	NA[d]
89.7	Cl^-	2.5	37 ± 2	7.5 ± 0.4
97.5	Cl^-	3.0	90 ± 50	NA[d]
80.2	I^-	1.6	12 ± 4	NA[d]
89.7	I^-	2.5	16.0 ± 1.0	0.87 ± 0.01
97.7	I^-	2.3	17.3 ± 1.4	NA[d]

[a]The HCO_3^-/CO_3^{2-} form was obtained from exposure of the OH⁻ form to ambient atmosphere. [b]Ion conductivity. [c]Water-soluble material. [d]Not measured.

backbone) is determined by the relative ratio of *x*, *y*, and *z* units, which in turn is determined by the degree of methylation (dm).[16]

The samples consisted of polymer films that were cast from dimethyl sulfoxide (DMSO) solutions formed by dissolving 0.20 g of polymer in 12 mL of hot DMSO. The resulting solutions were filtered into clean, flat Petri dishes and allowed to dry at 86 °C for 48 h in air. The resulting transparent, brown films were removed by addition of water, which allowed films to be peeled off of the glass. They were then transferred into deionized water for at least 48 h. The final films were approximately 50 μm thick. The films were cast in iodide form. Some of the films were treated with potassium chloride or potassium hydroxide to exchange the iodide for chloride or hydroxide.

Samples resulting from casting of HMT-PMBI with four different degrees of methylation (dm) of the N sites of the submolecular units were investigated in this study. Samples were measured in the original iodide form or after exchanging the iodide for chloride. The degree of methylation of the polymers ranged from 65.9 to 97.5% dm; a sample with a degree of methylation of 50%, is entirely uncharged and contains only (a) units. Table 1 reports values for the degree of methylation, ion exchange capacity (IEC) for the dry membrane, water uptake, and ion conductivity.[16,17] The OH⁻ form of the polymer was air-equilibrated with the result that the anion was in mixed hydroxide−carbonate form. ¹H NMR spectroscopy was used to determine the degree of methylation, from which the IEC was calculated. For 97.5% and 80.7% dm HMT-PMBI in chloride and iodide form, hydrated weight was measured after soaking in deionized water for 16 h at ambient temperature. Dry weight was measured after drying the samples

for 24 h at 353 K in a vacuum. The remaining material properties are reprinted from previous publications.[16,17]

X-ray scattering was performed using a SAXSLab Ganesha 300XL instrument. The instrument includes a copper anode source operating at 50 kV and 0.6 mA, producing Kα radiation with a wavelength λ = 1.54 Å, and a mobile PILATUS3 R 300 K photon counting detector. The entire instrument is housed in a 2 m vacuum chamber. Three scattering configurations—small-angle, medium-angle, and wide-angle X-ray scattering (SAXS, MAXS, and WAXS)—were achieved by moving the detector within the chamber, providing a usable *q*-range of 0.01−2.7 Å⁻¹, where $q = \frac{4\pi}{\lambda}\sin(\theta/2)$ is the scattering wave vector and θ is the scattering angle.

Samples were measured in a vacuum, in ambient conditions, and after hydration. Samples measured in a vacuum were affixed to a sample holder with double-sided tape and allowed to equilibrate within the evacuated instrument chamber for 1 h. Samples measured in ambient conditions were placed inside a paste cell consisting of an O-ring spacer and mica windows, which isolated the sample from the vacuum. Hydrated samples were submerged in water for 1 h, following which excess water was removed from the films by dabbing with tissue paper before they were placed in a paste cell. The stretched sample was prepared by drawing a film at room temperature and ambient humidity until it broke at an extension ratio of approximately 2. Portions of the stretched sample from near the tear point were measured in a vacuum.

A fitting function (eq S1) consisting of up to three pseudo-Voigt functions, a power law, and a *q*-independent background was fit to the data. The pseudo-Voigt function provides a flexible peak shape suitable for both crystalline and noncrystalline structure. The power law accounts for larger scale inhomogeneities in the sample. The measurement of wet 97.5% dm HMT-PMBI(Cl⁻) showed a mid-*q* feature. This was fit to the correlation length model (eq S2). Further details of analysis methods can be found in the Supporting Information. We assume that each visible peak corresponds to a single length scale in the material given by

$$d_i = 2.44 \times \frac{\pi}{q_i} \tag{1}$$

where q_i is the peak position, as recommended for scattering from amorphous polymers.[20]

Density functional theory (DFT) calculations were used to provide insight into the shape and electronic structure of the molecules. DFT calculations were performed using the Gaussian[21] quantum chemistry program, the B3LYP functional,[22] and the def2-TZVP basis set.[23] Figure 2 shows the
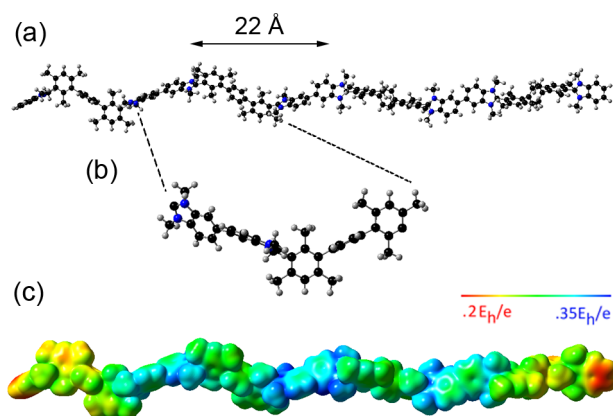

Figure 2. Results of the density functional theory calculation for fully methylated HMT-PMBI: (a) the optimized nuclei positions in a tetramer showing steric protection of the cationic region, (b) an expanded view of a single molecular unit, and (c) the electron density isosurface illustrating the relative hydrophilicity (blue) and hydrophobicity (green) of the molecule. The red areas are end effects due to the net positive charge of the molecule.

results of a geometry optimization of a cationic 100% dm HMT-PMBI tetramer at the B3LYP/def2-TZVP level of theory. Figure 2a shows the optimal nuclei positions; the molecule is highly extended, as it carries a net charge of +8 and is in a vacuum. The methylated, neutral aromatic rings are rotated approximately 80° out-of-plane relative to their corresponding cationic benzimidazolium units. This orientation sterically protects the most vulnerable carbon atom, the C2 carbon, which is located at the apex of the benzimidazole unit. This is in general agreement with calculations and measurements performed on small molecule analogues[18] and is believed to greatly contribute to the stability of the hydroxide form of HMT-PMBI. In analysis of methylated *m*-PBI and ether-linked PBI, the C2 carbon was found to be vulnerable to hydroxide attack.[24] Figure 2c shows the molecular electrostatic potential along an electron density isosurface of 0.002 electrons/a_0^3, where a_0 is the Bohr radius. The highest potential is concentrated along the nitrogen−carbon-nitrogen "triangle" of the benzimidazole rings. The mesitylene−phenylene−mesitylene group maintains a low and approximately constant potential. This confirms that this section of the molecule is hydrophobic. As this oligomer has a net electric charge of +8, the potential of the entire surface is positive.

Molecular dynamics (MD) simulations were designed to aid interpretation of the WAXS results.[25,26] Preliminary MD simulations were performed using the GPU-accelerated distribution of NAMD 2.11[27,28] with OPLS-AA-based parameters;[29] details can be found in the Supporting Information. Parameters are listed in Tables S1−S3; OPLS-AA parameters as implemented in NAMD were used when available. CHarMM36 parameters[30] where used for dihedral angles involving nitrogen methyl groups as no OPLS-AA parameters were available. The DFT results provided the atomic partial charges and initial geometries for the tetramers in the MD simulations.

RESULTS

X-ray scattering results for (a) HMT-PMBI(I⁻) and (b) HMT-PMBI(Cl⁻) samples of various dm in a vacuum are shown in Figure 3, plotted as a function of the magnitude of the
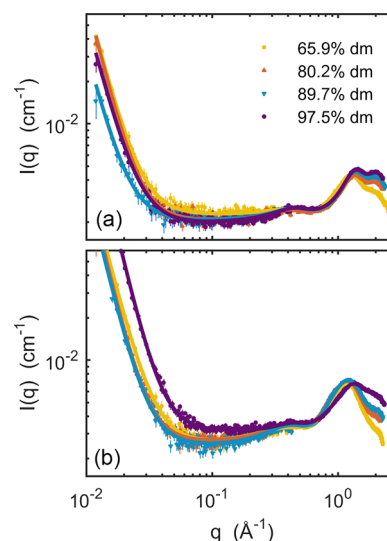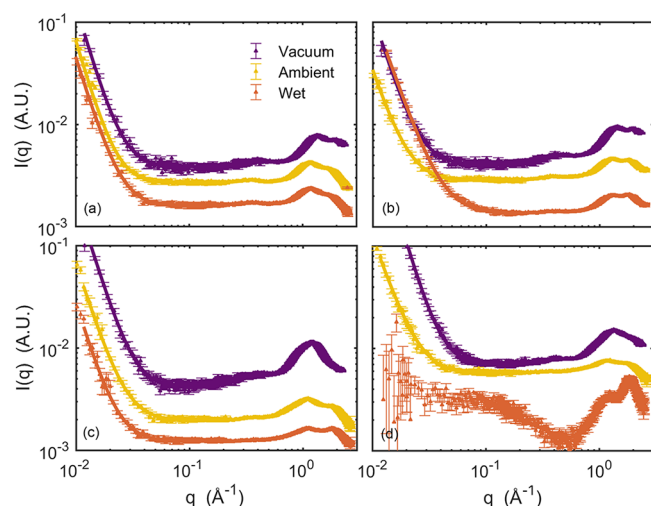

Figure 3. X-ray scattering profiles of films of (a) HMT-PMBI(I⁻) and (b) HMT-PMBI(Cl⁻) at degrees of methylation (dm) ranging from 65.9% to 97.5%, measured in a vacuum. The solid curves are fits of eq S1 to the data.

scattering wave vector, q. Three peaks are visible in each measurement: a small, broad peak at approximately 0.4 Å⁻¹ and two WAXS peaks, at approximately 1.35 and 2.00 Å⁻¹. We refer to these peaks as peak 0, peak 1, and peak 2, respectively; they correspond to length scales of approximately 20, 6.4, and 4 Å. Peak 2 increases in intensity with degree of methylation, while peak 0 and peak 1 show similar shape and intensity for different dm. Peak 2 is also much more clearly defined in the iodide form as compared to the chloride form of the polymer. The solid curves are fits of the model function to the data.

Figure 4 compares vacuum, ambient, and hydrated (wet) measurements for 80.2% and 97.5% dm HMT-PMBI in iodide and chloride form. All peaks shift to lower q with increased hydration, consistent with moderate swelling occurring during hydration. Peak 0 shrinks with increased hydration; it is no longer visible in the data for the wet chloride form samples. Except for the 80.2% dm HMT-PMBI(I⁻) sample, which uptakes little water, peak 2 increases in intensity with hydration. The measurement of hydrated 97.5% dm HMT-PMBI(Cl⁻), which uptakes a very large amount of water, shows a mid-q shoulder.

Figure 5 compares scattering from a stretched and an unstretched sample. Figure 5a shows the 2-D image of scattering from stretched 89.7% dm HMT-PMBI(I⁻) as captured by the detector. The stretched sample produced an anisotropic scattering pattern. For this image, the sample was mounted with the stretching axis along the vertical axis. The larger diameter complete ring, which corresponds to peak 1, shows stronger scattering in the direction perpendicular to the stretching axis, the equatorial direction. The smaller diameter partial ring, which corresponds to peak 0, shows stronger scattering in the direction parallel to the stretching axis, the meridional direction. To achieve a good coverage of q-space, it

Figure 4. X-ray scattering profiles of films of (a) 80.2% and (b) 97.5% dm HMT-PMBI(I⁻) and (c) 80.2% and (d) 97.5% dm HMT-PMBI(Cl⁻) at various levels of hydration: in a vacuum (purple), in ambient conditions (mustard), and fully hydrated (orange). In HMT-PMBI(Cl⁻), peak 2 significantly increases in intensity at ambient humidity and when hydrated. A vertical offset has been added to the data to reduce overlap.
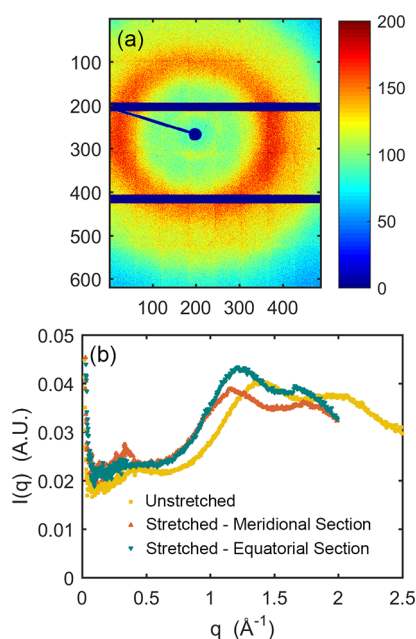
Figure 5. (a) Image from the 2-D detector and (b) integrated X-ray scattering from stretched and unstretched 89.7% dm HMT-PMBI(I⁻). Data for the unstretched sample are shown in yellow. Data for the stretched sample from meridional and equatorial sections are shown in orange and green, respectively.

was necessary to repeat the measurements after rotating the sample by 90°.

The results of the two measurements were combined into the profiles shown in Figure 5b by integrating 30° sections along the equatorial and meridional directions. In the stretched sample, peak 0 is significantly stronger and narrower in the meridional as compared to equatorial sections while the intensity of peak 1 is stronger in the equatorial as compared to the meridional sections. All peaks in the stretched sample are shifted to lower q than observed in the unstretched sample.

■ DISCUSSION

In all of the results shown in Figures 3−5, the small-angle behavior is dominated by a low-q upturn; there are no peaks or other obvious structural features visible in this q-range in most of our materials, indicating that no phase separation is occurring on length scales longer than a couple of nanometers. The exception is a small correlation knee in the most water-rich sample, 97.5% dm HMT-PMBI(Cl⁻). Small-angle neutron scattering results (described in the Supporting Information) confirm this observation.

All of the ionenes show two prominent WAXS peaks. Peak 1 corresponds to a length scale of approximately 6 Å while peak 2 corresponds to length scale of approximately 4 Å. Because peak 1 becomes stronger in the equatorial direction after stretching, we associate it with a backbone−backbone correlation length. As the film is stretched, the molecules become straighter and more parallel, enhancing the scattering in the direction perpendicular to the stretching direction.[20] Furthermore, there is a change in peak position; the peak in the data from the equatorial section appears at approximately 1.2 Å⁻¹, 10% below the position of peak 1 in the unstretched material. This is consistent with the difference in peak position between randomly oriented and parallel polymer chains with similar stacking lengths.[31]

We associate peak 2 with the ion−backbone and water−backbone spacings because the intensity of peak 2 is strongly correlated with both the degree of methylation and the water content of the material. Peak 2 dramatically increases in intensity and shifts to lower q when samples with greater degrees of methylation are hydrated, reflecting their large water uptake.

In the stretched material, the MAXS peak, peak 0, is not visible in the equatorial section and becomes more intense and shifts to lower q by approximately 25% (from 0.43 to 0.33 Å⁻¹) in the meridional section relative to the unstretched material. As the film is stretched and the polymer chains become more parallel, correlation between monomers should increase.[20] This suggests that peak 0 corresponds to a length scale along the polymer backbone, presumably a monomer−monomer correlation length with some contribution from the associated anions. The length scale associated with peak 0, approximately 20 Å, is slightly lower than the observed, fully extended monomer length in our DFT calculation, approximately 22 Å, highlighted in Figure 2. In previous work, we observed a similar peak in an uncharged benzimidazole-based material, again at a length scale corresponding to the expected monomer length.[32] We expect that the shift in peak position to lower q is caused by some combination of orientation and straightening of the polymer chains. A shift of up to 22% could be explained by a length scale shifting from isotropic to fully ordered, this is, the difference between the Debye and the Bragg lengths for amorphous and crystalline material, respectively.[31]

Fitting eq S1 to the data results in estimates for the length scales d_0, d_1, and d_2 associated with peaks 0, 1, and 2. The results are shown in Figure 6. Parts a and b show the length scale associated with peak 0, d_0, which we attribute to the monomer−monomer correlation length along the backbone. Parts c and d show the length scales associated with peak 1, d_1, which we attribute to the interbackbone spacing, and peak 2, d_2, which we attribute to the ion-backbone spacing. Parts a and c compare I⁻ samples at various levels of hydration—in a vacuum, in ambient conditions, and fully hydrated—for
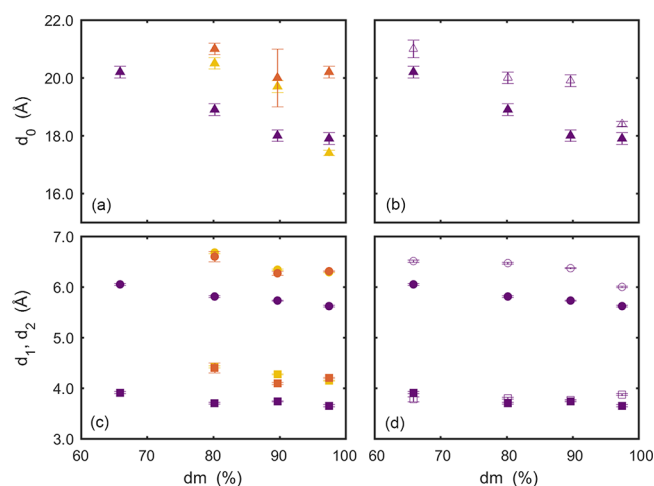
Figure 6. Length scales d_0, d_1, and d_2 associated with peaks 0, 1, and 2 obtained by fitting eq S1 to the data. (a) Comparison of d_0 for I^- form at various levels of hydration: in a vacuum (purple triangles), in ambient conditions (gold triangles), and fully hydrated (orange triangles). (b) Comparison of d_0 for I^- (closed triangles) and Cl^- (open triangles) forms. (c) Comparison of d_1 (circles) and d_2 (squares) for I^- form at various levels of hydration: in a vacuum (purple symbols), in ambient conditions (gold symbols), and fully hydrated (orange symbols). (d) Comparison of d_1 (circles) and d_2 (squares) for I^- (closed symbols) and Cl^- (open symbols) forms. The error bars are the uncertainties in the fit parameters.

samples of different charge content while parts b and d compare results for the I^- and Cl^- forms in a vacuum.

Methylation of the polymer impacts two of the three length scales. Increasing methylation has the most impact on the monomer–monomer correlation length, d_0. We believe that this correlation length becomes shorter with increasing

methylation because increased methylation results in the molecule becoming more constrained and hence less flexible. d_1 decreases slightly with increasing methylation; we postulate that the backbone–backbone distance gets smaller as packing becomes more efficient. While the amplitude of peak 2 (attributed to ion/water–backbone scattering) increases significantly with methylation, d_2 is independent of methylation.

Figures 6a and 6c show that all three length scales are 10–12% larger in ambient conditions relative to a vacuum; however, the differences between these length scales in ambient and fully hydrated samples are negligible. The increased length scales are consistent with swelling occurring in the presence of water. Hydration leads to larger monomer–monomer distances, backbone–backbone distances, and ion–backbone distances. The change in morphology at the nanoscale is consistent with dimensional measurements of 89.7% HMT-PMBI(I^-) which demonstrate a 30% increase in volume and a 10% increase in directional swelling.[17]

The monomer–monomer and backbone–backbone lengths depend on the anion, as shown in Figures 6b and 6d. The monomer–monomer length d_0 is 5% larger in Cl^- than I^- form while d_1 is 10% larger in Cl^- than I^- form. The smaller anion may allow the polymer backbone more freedom to elongate. However, d_2 does not change significantly with degree of methylation or counter-ion, suggesting that the anion–backbone distance is independent of charge content and roughly the same in Cl^- and I^- forms.

The measurement of wet 97.5% dm HMT-PMBI(Cl^-) shows a mid-q shoulder (Figure 4d). To associate a length scale with this feature, we fit the correlation length model (eq S2) to this region of the data resulting in a correlation length of 4.3 ± 0.3 Å. This feature is not present in any of the other samples or this sample at lower levels of hydration. This sample contains
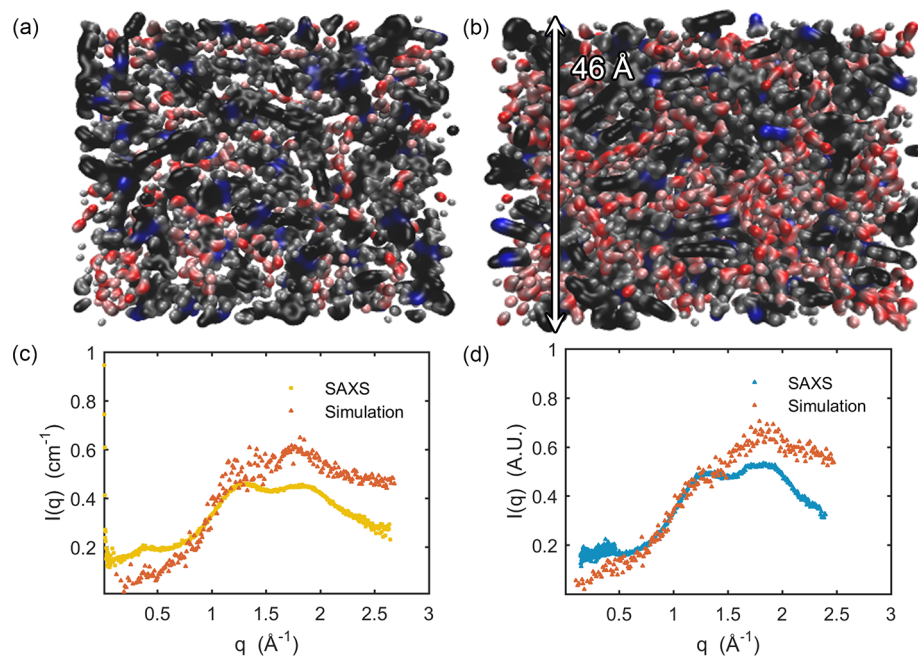
Figure 7. Results of the molecular dynamics simulation for a cell containing 25 100% dm tetramers for (a) 600 water molecules, corresponding to λ = 3, and (b) 1800 water molecules, corresponding to λ = 9. The colors represent carbon (black), nitrogen (blue), hydrogen (gray), oxygen (red), and iodide (pink). The structures correspond to surfaces of constant electron density. Parts c and d compare the structure factor calculated from the simulation data (orange) to the observed X-ray scattering profile for 97.5% dm HMT-PMBI(I^-) under (c) ambient conditions, λ = 3, (yellow) and (d) hydrated, λ = 9, (blue). The λ = 9 cell is approximately 46 Å tall, as indicated by the white arrow in part (b).

substantially more water than the others (Table 1); this appears to be the first indication of larger water-rich regions.

To confirm our interpretation of the scattering results, we performed molecular dynamics simulations using the NAnonscale Molecular Dynamics (NAMD) package for a fully methylated sample consisting of 25 tetramers. We compared results for 6 and 18 water molecules per monomer. Three water molecules per iodide ion ($\lambda = 3$) was chosen to represent material in ambient conditions, while 9 water molecules per iodide ($\lambda = 9$) was selected to represent the fully hydrated membrane. The equilibrated cell for $\lambda = 3$ had a density of 1.37 g/mL, while the cell for $\lambda = 9$ had a density of 1.35 g/mL, similar to the approximately 1.3 g/mL density of pristine PBI.

The results of our molecular dynamics simulation are shown in Figure 7. Figures 7a and 7b show the cell at the conclusion of the simulation; Figure 7a shows results for a cell at $\lambda = 3$, and Figure 7b shows results for a cell at $\lambda = 9$. The figures are estimated electron density isosurfaces produced by the VMD QuickSurf representation:[33] (black), nitrogen (blue), hydrogen (gray), oxygen (red), and iodide (pink). The polymer chains, shown as blue, black, and gray isosurfaces, appear to be randomly oriented, and as in the scattering data, no long-range order is visible. The water molecules, shown as red and gray isosurfaces, appear to form a network connecting the anions, shown in pink, and the cationic sites to each other. Remarkably, the distance between the backbones is similar in the two cells; the water forms strands in the $\lambda = 3$ cell, while it fills all of the empty space in the $\lambda = 9$ cell but, in either case, a network is formed. The percolating network, and lack of discrete ion clusters, is similar to what was observed by Frischknecht et al. in coarse-grained simulations of model ionenes.[34,35] In that research, ionenes were found to readily form percolating networks while pendant ionomers tended to be characterized by the presence of ionic aggregates.

Figures 7c and 7d compare the structure factor of the (c) $\lambda = 3$ and (d) $\lambda = 9$ simulation cells to the experimentally observed X-ray scattering profiles of 97.5% dm HMT-PMBI(I$^-$) under ambient and wet conditions, where it has similar water contents. The three peaks observed in the scattering profiles are reproduced by the simulation. While the relative intensities of the peaks are different, this is an expected consequence of neglecting the form factors of the atoms. Several individual correlation functions were also calculated from the data; these are included in the Supporting Information as Figure S3. Examination of the correlation functions confirms our interpretation of peaks 0, 1, and 2.

The ability of the polymer to form a network of hydrophilic pores is an important feature of the conductivity of these materials, which is higher than expected for a truly random polymer system. A polymer such as HMT-PMBI that becomes glassy during solution casting will not necessarily collapse to the optimal packing, and some space will be left behind, as is reported in polyimide materials.[36] This affect may be enhanced by casting in iodide form, as iodide is a particularly bulky ion. In fact, films cast from polymer in the iodide form uptake significantly less water than they do after exchange with other ions.[17]

CONCLUSIONS

We have investigated the morphology of a novel series of anion-conducting polymers, HMT-PMBI, with degrees of methylation ranging from 65.9% to 97.5%. Our studies included X-ray and neutron scattering, supplemented by gas-phase density functional theory calculations for the series and molecular dynamics simulations of a 25 tetramer cell for the fully methylated form. Length scales associated with the intramolecular monomer−monomer spacing, backbone−backbone, and ion−backbone spacings were identified in the scattering data and were consistent with simulation results. This represents the first structural investigation of these promising materials.

The small peak at midscattering angles, labeled peak 0, has been assigned to an intramolecular monomer−monomer spacing. In HMT-PMBI(I$^-$) samples, the peak corresponds to a length scale of 17.6−20.4 Å and slightly higher for chloride-form materials. The value for 97.5% dm in the iodide form is similar to the result calculated for the length of the central monomer in the gas-phase DFT calculation, 22 Å. These calculations, where the monomers are in a vacuum, are performed on fully methylated HMT-PMBI, shown in Figure 2. This interpretation is strengthened by the effect of stretching on the 89.7% dm HMT-PMBI(I$^-$) sample, as this peak is suppressed in the equatorial direction and both sharpened and shifted from 0.43 to approximately 0.33 Å^{-1} in the meridional direction. The effect of stretching the polymer is analogous to combing: it is expected that the chains would be straightened and preferably oriented in the direction parallel to the stretching.

We have assigned the WAXS peaks to angstrom-scale correlations between adjacent polymer chains, ions, and water molecules. We conclude that the highest-q peak (peak 2) corresponds to correlation between the backbones, halogens, and water. This is supported by a number of factors, the most obvious being that it increases in strength with IEC, and both increases in strength and shifts to lower q when the material is hydrated. A similar length scale is shown in the molecular dynamics simulation, where the iodide−oxygen and oxygen−oxygen spacings are shown to be shorter than the iodide−carbon length scale. We have assigned the first WAXS peak (peak 1) to both packing between backbone atoms in adjacent chains and correlation between ion−water channels. These features are visible at the ~6 Å length scale in the simulation, and it is common in the literature to assign the first clear WAXS peak to interchain stacking in polymers.[31] Furthermore, it strengthens relative to the higher-q peak as the degree of methylation is lowered. This interpretation is also strengthened by the effect of stretching on the WAXS profile; the peak shifted to lower q in the stretched material and sharpened in the equatorial direction.

Samples containing a moderate amount of water (<40%) showed no other features in their scattering profiles. When fully hydrated, the 97.5% dm HMT-PMBI(Cl$^-$) showed structure corresponding to a correlation length of 4.3 Å. These results show that even when hydrated, these materials contain no phase separation or water clustering on length scales greater than 6 Å and no characteristic length scales at all above the monomer length. This is uncommon among high-performance fuel cell membranes. MD simulations indicate that the water and ions in the membrane form an interpenetrating network where conductivity can occur.

ASSOCIATED CONTENT

Ⓢ Supporting Information

The Supporting Information is available free of charge on the ACS Publications website at DOI: 10.1021/acs.jpcb.7b10177.

Details of simulations; neutron scattering results; detailed description of analysis of X-ray scattering data; parameters obtained by fitting the model function to the X-ray scattering data (PDF)

■ AUTHOR INFORMATION

Corresponding Author

*E-mail: frisken@sfu.ca (B.J.F.).

ORCID ⊚

Barbara J. Frisken: 0000-0001-7234-891X

Notes

The authors declare no competing financial interest.

■ REFERENCES

(1) Marini, S.; Salvi, P.; Nelli, P.; Pesenti, R.; Villa, M.; Berrettoni, M.; Zangari, G.; Kiros, Y. Advanced Alkaline Water Electrolysis. *Electrochim. Acta* **2012**, *82*, 384−391.

(2) Krol, J.; Wessling, M.; Strathmann, H. Concentration Polarization with Monopolar Ion Exchange Membranes: Current-Voltage Curves and Water Dissociation. *J. Membr. Sci.* **1999**, *162*, 145−154.

(3) Kreuer, K.-D. Ion Conducting Membranes for Fuel Cells and Other Electrochemical Devices. *Chem. Mater.* **2014**, *26*, 361−380.

(4) Gellett, W.; Schumacher, J.; Kesmez, M.; Le, D.; Minteer, S. D. High Current Density Air-Breathing Laccase Biocathode. *J. Electrochem. Soc.* **2010**, *157*, B557−B562.

(5) Varcoe, J. R.; Atanassov, P.; Dekel, D. R.; Herring, A. M.; Hickner, M. A.; Kohl, P. A.; Kucernak, A. R.; Mustain, W. E.; Nijmeijer, K.; Scott, K.; et al. Anion-Exchange Membranes in Electrochemical Energy Systems. *Energy Environ. Sci.* **2014**, *7*, 3135−3191.

(6) Pan, J.; Chen, C.; Zhuang, L.; Lu, J. Designing Advanced Alkaline Polymer Electrolytes for Fuel Cell Applications. *Acc. Chem. Res.* **2012**, *45*, 473−481.

(7) Neagu, V.; Bunia, I.; Plesca, I. Ionic Polymers VI. Chemical Stability of Strong Base Anion Exchangers in Aggressive Media. *Polym. Degrad. Stab.* **2000**, *70*, 463−468.

(8) Dekel, D. R. Review of Cell Performance in Anion Exchange Membrane Fuel Cells. *J. Power Sources* **2018**, *375*, 158−169.

(9) Zhang, Q.; Li, S.; Zhang, S. A Novel Guanidinium Grafted Poly (Aryl Ether Sulfone) for High-Performance Hydroxide Exchange Membranes. *Chem. Commun.* **2010**, *46*, 7495−7497.

(10) Faraj, M.; Elia, E.; Boccia, M.; Filpi, A.; Pucci, A.; Ciardelli, F. New Anion Conducting Membranes Based on Functionalized Styrene-Butadiene-Styrene Triblock Copolymer for Fuel Cells Applications. *J. Polym. Sci., Part A: Polym. Chem.* **2011**, *49*, 3437−3447.

(11) Guo, M.; Fang, J.; Xu, H.; Li, W.; Lu, X.; Lan, C.; Li, K. Synthesis and Characterization of Novel Anion Exchange Membranes Based on Imidazolium-Type Ionic Liquid for Alkaline Fuel Cells. *J. Membr. Sci.* **2010**, *362*, 97−104.

(12) Gu, F.; Dong, H.; Li, Y.; Sun, Z.; Yan, F. Base Stable Pyrrolidinium Cations for Alkaline Anion Exchange Membrane Applications. *Macromolecules* **2014**, *47*, 6740−6747.

(13) Zhang, B.; Gu, S.; Wang, J.; Liu, Y.; Herring, A. M.; Yan, Y. Tertiary Sulfonium as a Cationic Functional Group for Hydroxide Exchange Membranes. *RSC Adv.* **2012**, *2*, 12683−12685.

(14) Gu, S.; Cai, R.; Luo, T.; Chen, Z.; Sun, M.; Liu, Y.; He, G.; Yan, Y. A Soluble and Highly Conductive Ionomer for High-Performance Hydroxide Exchange Membrane Fuel Cells. *Angew. Chem., Int. Ed.* **2009**, *48*, 6499−6502.

(15) Zha, Y.; Disabb-Miller, M. L.; Johnson, Z. D.; Hickner, M. A.; Tew, G. N. Metal-Cation-Based Anion Exchange Membranes. *J. Am. Chem. Soc.* **2012**, *134*, 4493−4496.

(16) Wright, A. G.; Holdcroft, S. Hydroxide-Stable Ionenes. *ACS Macro Lett.* **2014**, *3*, 444−447.

(17) Wright, A. G.; Fan, J.; Britton, B.; Weissbach, T.; Lee, H.-F.; Kitching, E. A.; Peckham, T. J.; Holdcroft, S. Hexamethyl-p-Terphenyl Poly (Benzimidazolium): a Universal Hydroxide-Conducting Polymer for Energy Conversion Devices. *Energy Environ. Sci.* **2016**, *9*, 2130−2142.

(18) Wright, A. G.; Weissbach, T.; Holdcroft, S. Poly (Phenylene) and m-Terphenyl as Powerful Protecting Groups for the Preparation of Stable Organic Hydroxides. *Angew. Chem., Int. Ed.* **2016**, *55*, 4818−4821.

(19) Shin, D. W.; Guiver, M. D.; Lee, Y. M. Hydrocarbon-Based Polymer Electrolyte Membranes: Importance of Morphology on Ion Transport and Membrane Stability. *Chem. Rev.* **2017**, *117*, 4759−4805.

(20) Roe, R.-J. *Methods of X-Ray and Neutron Scattering in Polymer Science*; Oxford University Press: 2000.

(21) Frisch, M. J.; et al. *Gaussian 09, Revision D*; Gaussian, Inc.: 2009.

(22) Becke, A. D. A New Mixing of Hartree-Fock and Local Density-Functional Theories. *J. Chem. Phys.* **1993**, *98*, 1372−1377.

(23) Schäfer, A.; Horn, H.; Ahlrichs, R. Fully Optimized Contracted Gaussian Basis Sets for Atoms Li to Kr. *J. Chem. Phys.* **1992**, *97*, 2571−2577.

(24) Henkensmeier, D.; Cho, H.; Brela, M.; Michalak, A.; Dyck, A.; Germer, W.; Duong, N. M. H.; Jang, J. H.; Kim, H.-J.; Woo, N.-S.; et al. Anion Conducting Polymers Based on Ether Linked Polybenzimidazole (PBI-OO). *Int. J. Hydrogen Energy* **2014**, *39*, 2842−2853.

(25) McDermott, A. G.; Larsen, G. S.; Budd, P. M.; Colina, C. M.; Runt, J. Structural Characterization of a Polymer of Intrinsic Microporosity: X-ray Scattering with Interpretation Enhanced by Molecular Dynamics Simulations. *Macromolecules* **2011**, *44*, 14−16.

(26) Perry, K. A.; More, K. L.; Payzant, A. E.; Meisner, R. A.; Sumpter, B. G.; Benicewicz, B. C. A Comparative Study of Phosphoric Acid-Doped m-PBI Membranes. *J. Polym. Sci., Part B: Polym. Phys.* **2014**, *52*, 26−35.

(27) Phillips, J. C.; Braun, R.; Wang, W.; Gumbart, J.; Tajkhorshid, E.; Villa, E.; Chipot, C.; Skeel, R. D.; Kale, L.; Schulten, K. Scalable Molecular Dynamics with NAMD. *J. Comput. Chem.* **2005**, *26*, 1781−1802.

(28) Kalé, L.; Skeel, R.; Bhandarkar, M.; Brunner, R.; Gursoy, A.; Krawetz, N.; Phillips, J.; Shinozaki, A.; Varadarajan, K.; Schulten, K. NAMD2: Greater Scalability for Parallel Molecular Dynamics. *J. Comput. Phys.* **1999**, *151*, 283−312.

(29) Jorgensen, W. L.; Maxwell, D. S.; Tirado-Rives, J. Development and Testing of the OPLS All-Atom Force Field on Conformational Energetics and Properties of Organic Liquids. *J. Am. Chem. Soc.* **1996**, *118*, 11225−11236.

(30) Vanommeslaeghe, K.; Hatcher, E.; Acharya, C.; Kundu, S.; Zhong, S.; Shim, J.; Darian, E.; Guvench, O.; Lopes, P.; Vorobyov, I.; et al. CHARMM General Force Field: A force field for drug-like molecules compatible with the CHARMM all-atom additive biological force fields. *J. Comput. Chem.* **2010**, *31*, 671−690.

(31) Alexander, L. E. *X-ray Diffraction Methods in Polymer Science*; John Wiley & Sons, Inc.: 1969.

(32) Schibli, E. M. Analysis of Novel Ionenes via X-ray and Neutron Scattering. M.Sc. Thesis, Simon Fraser University, 2016.

(33) Krone, M.; Stone, J.; Ertl, T.; Schulten, K. Fast Visualization of Gaussian Density Surfaces for Molecular Dynamics and Particle System Trajectories. EuroVis - Short Papers, 2012; pp 67−71.

(34) Hall, L. M.; Stevens, M. J.; Frischknecht, A. L. Effect of Polymer Architecture and Ionic Aggregation on the Scattering Peak in Model Ionomers. *Phys. Rev. Lett.* **2011**, *106*, 127801.

(35) Hall, L. M.; Seitz, M. E.; Winey, K. I.; Opper, K. L.; Wagener, K. B.; Stevens, M. J.; Frischknecht, A. L. Ionic Aggregate Structure in Ionomer Melts: Effect of Molecular Architecture on Aggregates and the Ionomer Peak. *J. Am. Chem. Soc.* **2012**, *134*, 574−587.

(36) Marestin, C.; Gebel, G.; Diat, O.; Mercier, R. Sufonated Polyimides. *Adv. Polym. Sci.* **2008**, *216*, 185−258.

Supporting information for:

Morphology of Anion-Conducting Ionenes Investigated by X-ray Scattering and Simulation

Eric M. Schibli,[†] Andrew G. Wright,[‡] Steven Holdcroft,[‡] and Barbara J. Frisken[*,†]

[†]Department of Physics, Simon Fraser University, Burnaby BC Canada V5A 1S6

[‡]Department of Chemistry, Simon Fraser University, Burnaby BC Canada V5A 1S6

E-mail: frisken@sfu.ca

Molecular Dynamics Simulations

The molecular model is shown in Fig. S1.
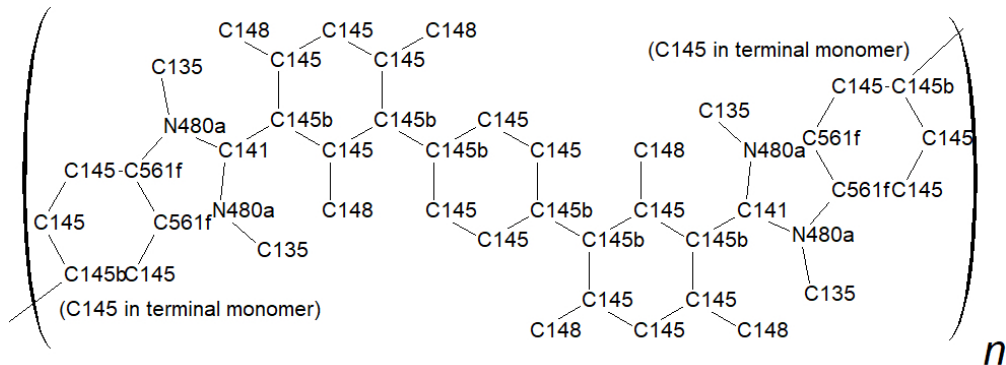
Figure S1: A monomer of 100% dm HMT-PMBI, labeled with the atom types. Hydrogens are excluded from this figure. Hydrogens in the methyl groups bonded to nitrogen are labeled H911, those in methyl groups bonded to carbon are labeled H140, and those bonded to aromatic carbons are labeled H146.

We used the Optimized Parameters for Liquid Simulations - All Atoms (OPLS-AA) force field distributed with NAMD 2.11 for the MD simulations,[S1] where available. Non-bonded parameters for iodide were taken from Ref. S2, and the final eight dihedral parameters, related to twisting between benzimidazolium and mesitylene groups and to twisting between the benzimidazolium methyl groups, were taken from the CHARMM general force field.[S3] The parameters we used are tabulated in Tables S1, S2 and S3.

Atomic partial charges for the simulation were assigned according to the CHELPG (CHarges from Electrostatic Potentials using a Grid-based method) scheme, in which the atomic charges are fit to the molecular electrostatic potential on a 3 pm rectangular grid of points surrounding the molecule.[S4] This charge distribution is depicted in Fig. S2. This procedure was used to produce partial charges in a recent simulation of acid-doped PBI.[S5] The grid excludes points within the van der Waals radius of any atom, and includes 28 pm of extra space around the molecule in each dimension. This represents a second departure from the procedure of Ref. S6, in which the atomic charges of each accessible atom are fit to the atom's interaction energies with water. This would also have been very expensive,

Table S1: OPLS-AA bond-stretching parameters for 100% dm HMT-PMBI(I$^-$).

Atom	Atom	K_r (kcal/mol/Å^2)	r_0 (Å)
C141	C145	392.00	1.400
C141	N480a	375.000	1.365
N480a	C561f	375.000	1.365
N480a	C135	320.000	1.448
C561f	C561f	392.00	1.400
C561f	C145	392.00	1.400
C145	C145B	392.00	1.400
C145	H146	307.000	1.080
C145B	C145B	392.00	1.400
C145	C145	392.00	1.400
C135	H911	285.00	1.090
C145	C148	365.00	1.510
C148	H140	340.000	1.090
OT	HT	450.0	0.9572
HT	HT	0.0	1.5139

and unlikely to give good results, as the most highly charged atoms in HMT-PMBI are not accessible to water.
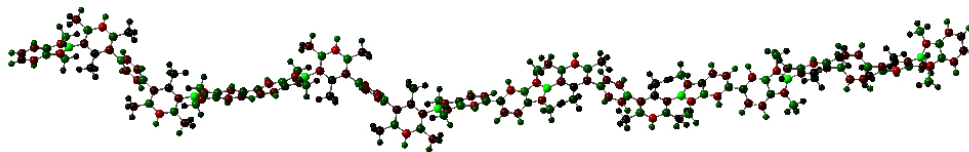
Figure S2: Atomic partial charges. Green nuclei were assigned more positive charges; red nuclei, negative charges. The bulk of the charge appearing in the apex carbon of the imidazole ring is in agreement with an investigation of similar materials in Ref. S7.

Molecular dynamics simulations were performed using NAMD 2.10.[S8] The initial configuration of the 25 tetramers was produced using Packmol.[S9] The energy was then minimized using a conjugate-gradient algorithm, and the cell was annealed at 1000 K for 1 ns at constant volume. The cell size was then reduced to $80 \times 80 \times 80$ Å^3 (representing a density of 0.35 g/ml), periodic boundaries were added, and the system was then cooled to 800 K and annealed for a further 20 ns at constant pressure (1 atm). Subsequently, water and counter-ions were added, again using Packmol, and the system was energy-minimized and

Table S2: OPLS-AA angle-bending parameters for 100% dm HMT-PMBI(I$^-$).

Atom	Atom	Atom	K_θ (kcal/mol/rad^2)	θ_0 (°)
C141	N480a	C135	70.00	125.000
C141	N480a	C561f	70.00	125.000
N480a	C561f	C145	70.00	108.000
N480a	C561f	C561f	70.00	108.000
N480a	C141	C145	70.00	108.000
N480a	C141	N480a	70.00	123.000
N480a	C135	H911	35.00	109.000
C561f	C145	H146	35.00	109.500
C561f	N480a	C135	50.00	118.000
C145	C148	H140	33.00	109.500
C145	C145	C148	70.00	120.000
C145B	C145	C148	70.00	120.000
C145B	C145	H146	35.00	109.500
C145	C145	H146	35.00	120.000
H140	C148	H140	33.00	107.800
H911	C135	H911	33.00	107.800
C561f	C145	C145	63.00	120.000
C145B	C145	C145	63.00	120.000
C145	C145B	C145B	63.00	120.000
C145	C145B	C145	63.00	120.000
C141	C145	C145	63.00	120.000
C561f	C145	C145B	63.00	120.000
C561f	C561f	C145	63.00	120.000
C145	C145	C145	63.00	120.000
HT	OT	HT	55.0	104.52

annealed at 500 K for an additional 20 ns at 1 atm, and then cooled to 298 K in 1 K, 5 ps steps. To prevent large temperature gradients from appearing during the cooling phase, velocities were reassigned to match the thermostat temperature at each step. Finally, the cell was equilibrated for 50 ns, and sampling was performed over an additional 150 ns of simulation. Constant pressure simulations were performed via the Noosé-Hoover Langevin piston method,[S10] using periodic boundary conditions. The relaxation time was set to 0.2 ps, the damping coefficient was set to 5 ps^{-1}, and the integration timestep was set to 1 fs, the default values in NAMD.

Pair-Correlation Functions

Pair-correlation functions describe the probability of finding a particle at a distance r from a reference particle. We used pair-correlation functions to provide insight into the origins of the three length scales visible in the scattering profiles. Results for pair-correlation functions calculated using VMD[S11] for the equilibrated simulation cells are shown in Fig. S3. Calculations included correlations between iodide ions and carbon and nitrogen atoms (iodide-backbone), between oxygen atoms and carbon and nitrogen atams (water-backbone), between carbon and nitrogen atoms that are not members of the same chain (backbone-backbone), between water and iodide, and between members of imidazole rings in the same chain (imidazole-imidazole). Hydrogen atoms were not considered in this calculation because they do not contribute meaningfully to the scattering. The pair-correlation functions are not weighted by scattering cross-sections. The results were averaged over the sampling phase. Iodide-polymer and water-polymer are shown as one curve because the two correlation functions are similar. The results show that length scales associated with Peaks 0, 1 and 2 from the calculated structure factor, as labeled in Fig. S3, correspond to either a peak or a shoulder in the pair-correlation functions. In Figs. S3 (a) and (b), the correlation structure associated with iodide-backbone, water-backbone and iodide-water curves corresponds to the location of Peak 2, while the correlation structure associated with the backbone-backbone curve corresponds to the location of Peak 1, as identified on the figure. The first peak in Figs. S3 (c) and (d) corresponds to spacing between adjacent imidazole rings, while the peak at approximately 20 Å corresponds to the monomer-monomer spacing.

Cluster Analysis

A cluster analysis was performed[S12] to confirm that the water and ions formed a percolating network in our simulation results. Atoms within 3 Å were considered to be part of the same cluster. The results were averaged over 100 frames separated by 1.5 ns. The results are
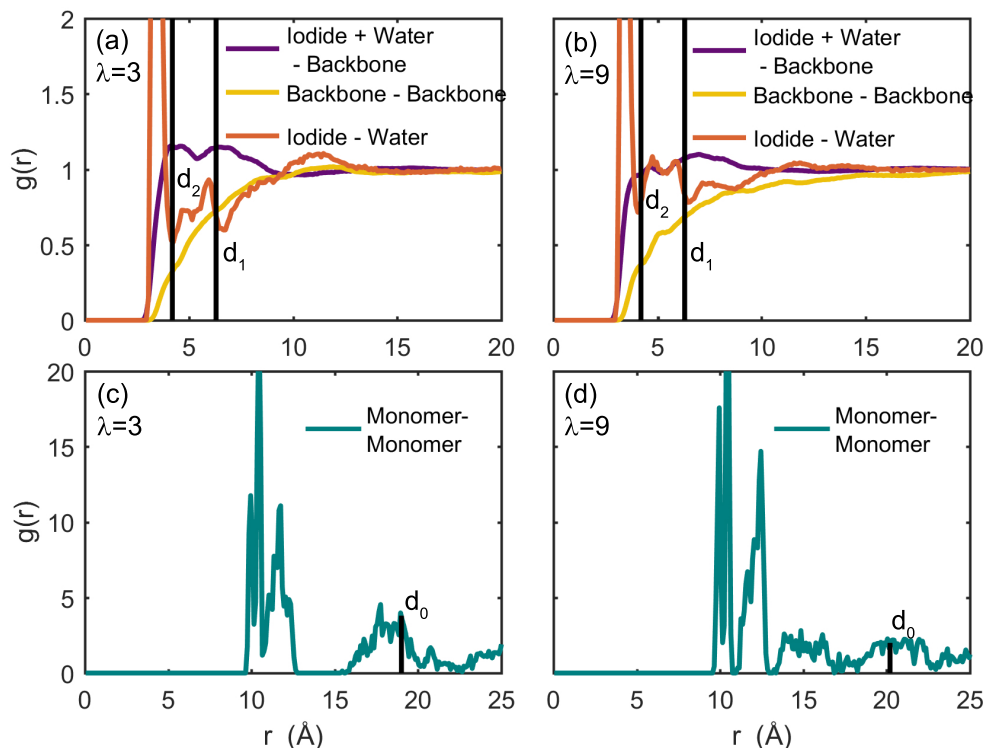
Figure S3: Results for pair-correlation functions calculated from the MD simulations for the $\lambda = 3$ cell are shown in (a) and (c) while results for the $\lambda = 9$ cell are shown in (b) and (d). Results for the iodide- and water-backbone and backbone-backbone correlations are shown in the top row (a and b), while results for monomer-monomer correlations are shown in the bottom row (c and d). The length scales estimated from scattering measurements of comparable samples are shown as black bars.

shown in Figs. S4 and S5.

Small-Angle Neutron Scattering

Exploratory small-angle neutron scattering (SANS) experiments were performed by our collaborator, Dr. Sandrine Lyonnard, at the Labratoire Léon Brillouin (Saclay, France). Samples were hydrated in either H_2O or D_2O to take advantage in the very different scattering lengths of protium and deuterium. Results for three HMT-PMBI(I$^-$) samples with dm = 65.9, 80.2 and 89.7 % are shown in Fig. S6. The data show a smooth transition from a power law at low q to a flat background at higher q when hydrated with either H_2O or D_2O. There are no peaks, knees, or other features associated with phase separation, consistent
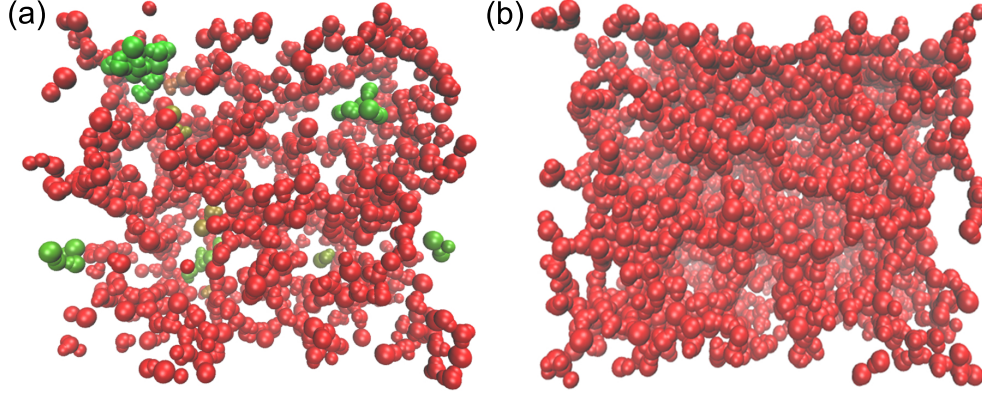
Figure S4: Results for cluster-analysis calculations performed on the MD simulations at (a) $\lambda = 3$ and (b) $\lambda = 9$. Iodide ions, water oxygens, and water hydrogens are shown as spheres of their van der Waals radii. The percolating network is shown in red, while particles that are isolated or part of smaller clusters are shown in green.

with the SAXS results for the same q-range. The vertical shift in the H_2O data relative to the D_2O data for the higher-IEC samples reflects the higher level of incoherent scattering by H_2O.

Analysis

As the form factor of the scatterers is not known a priori, we have selected a fitting function that combines a sum of three pseudo-Voigt functions—each a sum of a Gaussian and Lorentzian peak with the same positions and widths—with a single power law function with amplitude a_o and power p and a flat baseline b_o:[S13]

$$I(q) = a_o \cdot q^{-p} + \sum_i \left\{ s_i \cdot a_i \cdot \exp\left(-(2 \cdot (q - b_i)/c_i)^2 \cdot \log(2) \right) + \frac{a_i \cdot (1 - s_i)}{(1 + (2 \cdot ((q - b_i)/c_i)^2))} \right\} + b_o. \tag{1}$$

Psuedo-Voigt functions provide a flexible peak shape from a minimal number of parameters. The parameters a_i, b_i, c_i, and s_i define the peak height, position, full width at half max, and shape, respectively, of each peak. Both the frequency of occurrence of a length scale and the scattering factors of the scatterers contribute to the peak intensity. While the size
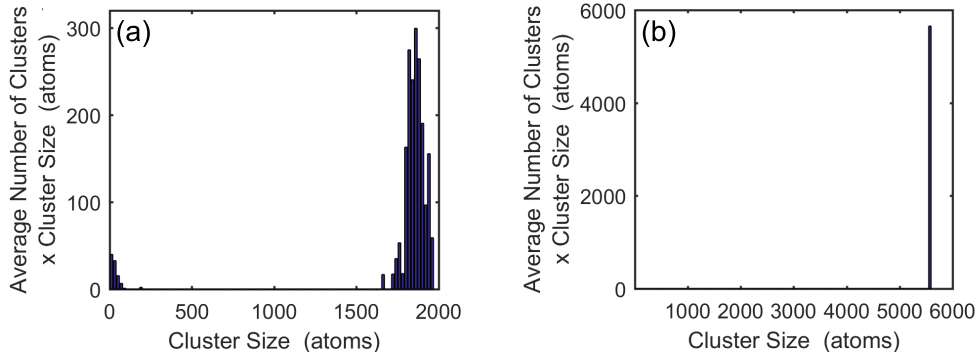
Figure S5: The results of the culster-analysis calculation showing the cluster size distribution for 100 frames of the MD simulation. The x-axis shows cluster size, while the y-axis shows average number of clusters of a given size, multiplied by the size of the clusters, in order to compare the distribution of atoms. (a) Results for λ=3 show that most atoms are part of a large cluster that averages 1800 atoms in size. (b) Results for λ=0 show that all atoms are part of a single cluster in each sample of the MD simulation.

of crystallites may be inferred from c_i through the Debye-Sherrer formula—which states crystallite diameter is inversely proportional to peak width[S14]—as we only observed non-crystalline peaks, we did not consider peak width quantitatively; rather, we assumed a broader peak indicated a less well-defined length scale. $s_i = 1$ corresponds to a pure Gaussian peak, while $s_i = 0$, to a completely Lorentzian peak.

The mid-q feature in the 97.5% dm HMT-PMBI(Cl-) data was fit to the correlation length model as implemented in the NIST small-angle scattering package[S15]

$$I(q) = \frac{A}{q^n} + \frac{C}{1 + (q\xi)^m} + B \quad , \tag{2}$$

where ξ is the correlation length, A and C are scale parameters, n is the exponent associated with the low-q power law, m describes the shape of the shoulder, and B is the q-independent background.

The fits were performed in three stages, each using MATLAB 2014b's weighted trust-region nonlinear least-squares fit procedure. First, the data below the first (local) intensity minimum was fit to $a_o \cdot q^p + b_o$. The result was then subtracted from the remaining data, and the difference was fit to a sum of Gaussian peaks. The resulting fit parameters were

S8

then used as a starting point to fit Equation 1 to the full range of the original data. Finally, a Monte Carlo algorithm was used to estimate the uncertainty in each fit parameter using uncertainties for each datapoint as reported by SAXSGUI. Results are tabulated in Tables S4, S5, S6, S7, S8, and S9.

Parameters determined from fits of Eq. 1 to the data

We assume that each visible peak corresponds to a single length scale in the material

$$d \ = \ 2.44 \times \frac{\pi}{q} \tag{3}$$

as recommended for broad amorphous peaks.[S16] Results are tabulated in Tables S10, S11, and S12.

References

(S1) Jorgensen, W. L.; Maxwell, D. S.; Tirado-Rives, J. Development and Testing of the OPLS All-Atom Force Field on Conformational Energetics and Properties of Organic Liquids. *J. Am. Chem. Soc.* **1996**, *118*, 11225–11236.

(S2) Jensen, K. P.; Jorgensen, W. L. Halide, Ammonium, and Alkali Metal Ion Parameters for Modeling Aqueous Solutions. *J. Chem. Theory Comput.* **2006**, *2*, 1499–1509.

(S3) Vanommeslaeghe, K.; Hatcher, E.; Acharya, C.; Kundu, S.; Zhong, S.; Shim, J.; Darian, E.; Guvench, O.; Lopes, P.; Vorobyov, I.; et al., CHARMM General Force Field: A Force Field for Drug-Like Molecules Compatible with the CHARMM All-Atom Additive Niological Force Fields. *J. Comput. Chem.* **2010**, *31*, 671–690.

(S4) Breneman, C. M.; Wiberg, K. B. Determining Atom-Centered Monopoles from Molec-

ular Electrostatic Potentials. The Need for High Sampling Density in Formamide Conformational Analysis. *J. Comput. Chem.* **1990**, *11*, 361–373.

(S5) Zhu, S.; Yan, L.; Zhang, D.; Feng, Q. Molecular Dynamics Simulation of Microscopic Structure and Hydrogen Bond Network of the Pristine and Phosphoric Acid Doped Polybenzimidazole. *Polymer* **2011**, *52*, 881–892.

(S6) Mayne, C. G.; Saam, J.; Schulten, K.; Tajkhorshid, E.; Gumbart, J. C. Rapid Parameterization of Small Molecules Using the Force Field Toolkit. *J. Comput. Chem.* **2013**, *34*, 2757–2770.

(S7) Henkensmeier, D.; Cho, H.; Brela, M.; Michalak, A.; Dyck, A.; Germer, W.; Duong, N. M. H.; Jang, J. H.; Kim, H.-J.; Woo, N.-S.; et al., Anion Conducting Polymers Based on Ether Linked Polybenzimidazole (PBI-OO). *Int. J. of Hydrogen Energy* **2014**, *39*, 2842–2853.

(S8) Kalé, L.; Skeel, R.; Bhandarkar, M.; Brunner, R.; Gursoy, A.; Krawetz, N.; Phillips, J.; Shinozaki, A.; Varadarajan, K.; Schulten, K. NAMD2: Greater Scalability for Parallel Molecular Dynamics. *J. Comput. Phys.* **1999**, *151*, 283–312.

(S9) Martínez, L.; Andrade, R.; Birgin, E. G.; Martínez, J. M. Packmol: A package for building initial configurations for molecular dynamics simulations. *J. Comput. Chem.* **2009**, *30*, 2157–2164.

(S10) Feller, S. E.; Zhang, Y.; Pastor, R. W.; Brooks, B. R. Constant Pressure Molecular Dynamics Simulation: The LangevinPiston Method. *J. Chem. Phys.* **1995**, *103*, 4612–4621.

(S11) Humphrey, W.; Dalke, A.; Schulten, K. VMD – Visual Molecular Dynamics. *J. Mol. Graphics* **1996**, *14*, 33–38.

(S12) Hall, L. M.; Seitz, M. E.; Winey, K. I.; Opper, K. L.; Wagener, K. B.; Stevens, M. J.; Frischknecht, A. L. Ionic Aggregate Structure in Ionomer Melts: Effect of Molecular Architecture on Aggregates and the Ionomer Peak. *J. Am. Chem. Soc.* **2012**, *134*, 574–587, PMID: 22133577.

(S13) Rabiej, S. A Comparison of Two X-ray Diffraction Procedures for Crystallinity Determination. *Eur. Polym. J.* **1991**, *27*, 947–954.

(S14) Scherrer, P. *Kolloidchemie Ein Lehrbuch*; Springer, 1912; pp 387–409.

(S15) Kline, S. R. Reduction and analysis of SANS and USANS data using IGOR Pro. *Journal of applied crystallography* **2006**, *39*, 895–900.

(S16) Roe, R.-J. *Methods of X-Ray and Neutron Scattering in Polymer Science*; Oxford University Press, 2000.

Table S3: OPLS-AA/CHARMM dihedral-angle parameters for 100% dm HMT-PMBI(I⁻).

| Atom	Atom	Atom	Atom	K_ϕ (kcal/mol/rad²)	n	Offset (°)
X	C145	C145	X	3.6250	2	180.0
X	C561f	C561f	X	3.6250	2	180.0
C141	N480a	C135	H911	0.1500	3	180.00
C561f	N480a	C135	H911	0.1500	3	180.00
C145B	C145	C148	H140	0.1500	3	180.00
C145	C145	C148	H140	0.1500	3	180.00
N480a	C561f	C145	C145B	3.6250	2	180.0
N480a	C561f	C145	H146	3.6250	2	180.0
N480a	C141	C145	C145	3.6250	2	180.0
C561f	C561f	C145	C145B	3.6250	2	180.0
C561f	C561f	C145	H146	3.6250	2	180.0
C561f	C145	C145B	C145	3.6250	2	180.0
C561f	C145	C145B	C145B	3.6250	2	180.0
C561f	C561f	C145	C145	3.6250	2	180.0
C145	C145B	C145	C145	3.6250	2	180.0
C145	C145B	C145	H146	3.6250	2	180.0
C145	C145B	C145B	C145	3.6250	2	180.0
H146	C145	C145B	C145B	3.6250	2	180.0
C145B	C145B	C145	C145	3.6250	2	180.0
C145	C145B	C145	C148	3.6250	2	180.0
C145B	C145B	C145	C148	3.6250	2	180.0
N480a	C561f	C145	C145	3.6250	2	180.0
C141	N480a	C561f	C561f	12.0000	2	180.00
C141	N480a	C561f	C145	12.0000	2	180.00
N480a	C141	N480a	C561f	12.0000	2	180.00
C145	C141	N480a	C561f	12.0000	2	180.00
N480a	C141	N480a	C135	6.0000	2	180.00
C135	N480a	C561f	C561f	6.0000	2	180.00
C135	N480a	C561f	C145	6.0000	2	180.00
C145	C141	N480a	C135	6.0000	2	180.00
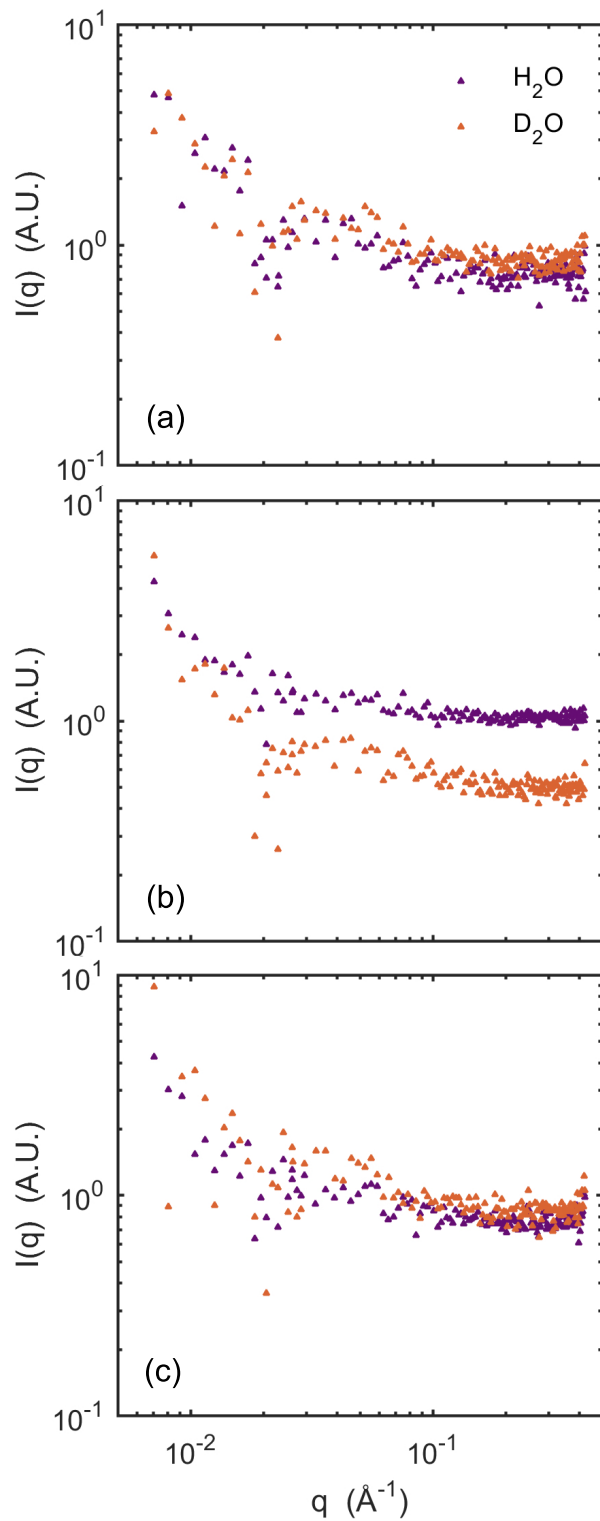
Figure S6: Small-angle neutron scattering results for the HMT-PMBI(I$^-$) membranes, (a) 65.9% dm, (b) 80.2%, and (c) 89.7%, plotted with logarithmic axes. These materials demonstrate a smooth transition from a power law at low q to a flat background at higher q. This is typical of amorphous polymers with no phase separation.

Table S4: Fit parameters for HMT-PMBI(I$^-$), measured in vacuum.

	97.5% dm	89.7% dm	80.2% dm	65.9% dm
a_1	$(4.9 \pm 0.4) \times 10^{-4}$	$(4.2 \pm 0.4) \times 10^{-4}$	$(3.9 \pm 0.4) \times 10^{-4}$	$(1.9 \pm 0.3) \times 10^{-4}$
b_1	0.429 ± 0.003	0.425 ± 0.005	0.406 ± 0.004	0.38 ± 0.01
c_1	0.43 ± 0.03	0.39 ± 0.04	0.38 ± 0.03	0.29 ± 0.04
s_1	0.1 ± 0.2	0 ± 0.3	0 ± 0.3	1 ± 0.4
a_2	$(2.7 \pm 0.2) \times 10^{-3}$	$(1.9 \pm 0.1) \times 10^{-3}$	$(2.2 \pm 0.1) \times 10^{-3}$	$(1.93 \pm 0.03) \times 10^{-3}$
b_2	1.365 ± 0.003	1.337 ± 0.002	1.319 ± 0.004	1.268 ± 0.003
c_2	0.76 ± 0.02	0.63 ± 0.02	0.69 ± 0.02	0.611 ± 0.008
s_2	0.11 ± 0.04	0.42 ± 0.08	0.38 ± 0.04	0.7 ± 0.06
a_3	$(2.24 \pm 0.09) \times 10^{-3}$	$2.3 \pm 0.1 \times 10^{-3}$	$(1.69 \pm 0.06) \times 10^{-3}$	$(9.6 \pm 0.4) \times 10^{-4}$
b_3	2.103 ± 0.008	2.05 ± 0.01	2.07 ± 0.01	1.959 ± 0.008
c_3	0.82 ± 0.07	1.11 ± 0.07	0.84 ± 0.06	0.83 ± 0.04
s_3	1.0 ± 0.3	0 ± 0.3	1 ± 0.2	0.6 ± 0.2
a_o	$(8 \pm 2) \times 10^{-9}$	$(3 \pm 3) \times 10^{-9}$	$(3 \pm 1) \times 10^{-9}$	$(1.0 \pm 0.5) \times 10^{-8}$
p	-3.43 ± 0.07	-3.5 ± 0.2	-3.68 ± 0.07	-3.4 ± 0.1
b_o	$(1.66 \pm 0.05) \times 10^{-3}$	$(1.74 \pm 0.06) \times 10^{-3}$	$(1.88 \pm 0.04) \times 10^{-5}$	$(2.2 \pm 0.5) \times 10^{-4}$

Table S5: Fit parameters for HMT-PMBI(Cl$^-$), measured in vacuum.

	97.5% dm	89.7% dm	80.2% dm	65.9% dm
a_1	$(2.8 \pm 0.2) \times 10^{-4}$	$(8.0 \pm 0.5) \times 10^{-4}$	$(7.1 \pm 0.4) \times 10^{-4}$	$(7 \pm 1) \times 10^{-4}$
b_1	0.416 ± 0.003	0.386 ± 0.003	0.383 ± 0.003	0.350 ± 0.005
c_1	0.23 ± 0.01	0.32 ± 0.01	0.31 ± 0.01	0.38 ± 0.05
s_1	1 ± 0.3	1.0 ± 0.1	1.0 ± 0.2	1.0 ± 0.3
a_2	$(3.2 \pm 0.1) \times 10^{-3}$	$(4.6 \pm 0.1) \times 10^{-3}$	0.0044 ± 0.0001	$(4.41 \pm 0.06) \times 10^{-3}$
b_2	1.280 ± 0.003	1.197 ± 0.004	1.179 ± 0.003	1.179 ± 0.003
c_2	0.764 ± 0.007	0.749 ± 0.007	0.721 ± 0.007	0.733 ± 0.008
s_2	0.69 ± 0.04	1.00 ± 0.02	0.96 ± 0.03	0.80 ± 0.06
a_3	$(2.23 \pm 0.05) \times 10^{-3}$	$(1.86 \pm 0.06) \times 10^{-3}$	$(1.29 \pm 0.06) \times 10^{-3}$	$(7 \pm 1) \times 10^{-4}$
b_3	2.03 ± 0.01	2.02 ± 0.01	1.99 ± 0.01	1.95 ± 0.01
c_3	0.98 ± 0.05	0.78 ± 0.06	0.75 ± 0.08	0.60 ± 0.09
s_3	1 ± 0.2	1.0 ± 0.3	1.0 ± 0.3	1.0 ± 0.3
a_o	$(1.3 \pm 0.2) \times 10^{-8}$	$(6 \pm 2) \times 10^{-9}$	$(4 \pm 1) \times 10^{-9}$	$(1.8 \pm 0.3) \times 10^{-8}$
p	-3.87 ± 0.03	-3.72 ± 0.07	-3.82 ± 0.06	-3.53 ± 0.04
b_o	$(3.06 \pm 0.03) \times 10^{-3}$	$0.00243 \pm 5.00E-05$	$(2.59 \pm 0.05) \times 10^{-3}$	$(2.3 \pm 0.1) \times 10^{-3}$

Table S6: Fit parameters for HMT-PMBI(I$^-$), ambient conditions.

	97.5% dm	89.7% dm	80.2% dm
a_1	$(3.5 \pm 0.5) \times 10^{-4}$	$(2.4 \pm 0.2) \times 10^{-4}$	$(1.55 \pm 0.08) \times 10^{-4}$
b_1	0.40 ± 0.03	0.389 ± 0.005	0.356 ± 0.002
c_1	0.19 ± 0.04	0.20 ± 0.03	0.18 ± 0.02
s_1	0.7 ± 0.3	0.9 ± 0.4	0.9 ± 0.2
a_2	$(2.4 \pm 0.3) \times 10^{-3}$	$(1.88 \pm 0.03) \times 10^{-3}$	$(1.23 \pm 0.01) \times 10^{-3}$
b_2	1.222 ± 0.005	1.209 ± 0.002	1.148 ± 0.003
c_2	0.52 ± 0.04	0.544 ± 0.007	0.533 ± 0.004
s_2	0.5 ± 0.1	0.53 ± 0.05	0.75 ± 0.03
a_3	$(3.9 \pm 0.1) \times 10^{-3}$	$(2.44 \pm 0.03) \times 10^{-3}$	$(7.74 \pm 0.09) \times 10^{-4}$
b_3	1.851 ± 0.008	1.796 ± 0.004	1.735 ± 0.004
c_3	1.2 ± 0.2	1.00 ± 0.02	0.64 ± 0.01
s_3	0 ± 0.2	0.00 ± 0.03	1.00 ± 0.05
a_o	$(1.0 \pm 0.4) \times 10^{-9}$	$(1.0 \pm 0.4) \times 10^{-9}$	$(1.00 \pm 0.06) \times 10^{-9}$
p	-3.63 ± 0.06	-3.65 ± 0.06	-3.86 ± 0.01
b_o	$(1.5 \pm 0.3) \times 10^{-3}$	$(1.69 \pm 0.04) \times 10^{-3}$	$(2.19 \pm 0.01) \times 10^{-4}$

Table S7: Fit parameters for HMT-PMBI(Cl$^-$), ambient conditions.

	97.5% dm	89.7% dm	80.2% dm
a_1	$(2 \pm 2) \times 10^{-4}$	$(1.5 \pm 0.8) \times 10^{-4}$	$(1.9 \pm 0.7) \times 10^{-4}$
b_1	0.35 ± 0.04	0.33 ± 0.03	0.33 ± 0.04
c_1	0.1 ± 0.2	0.58 ± 0.05	0.14 ± 0.02
s_1	1 ± 0.5	0.0 ± 0.3	1.0 ± 0.4
a_2	$(3.9 \pm 0.1) \times 10^{-3}$	$(4.3 \pm 0.1) \times 10^{-4}$	$(3.9 \pm 0.4) \times 10^{-4}$
b_2	1.164 ± 0.005	1.107 ± 0.002	1.070 ± 0.002
c_2	0.74 ± 0.03	0.78 ± 0.02	0.703 ± 0.006
s_2	0.2 ± 0.1	0.62 ± 0.07	0.59 ± 0.05
a_3	$(2.8 \pm 0.3) \times 10^{-3}$	$(3.1 \pm 0.1) \times 10^{-4}$	$(2.3 \pm 0.2) \times 10^{-4}$
b_3	1.880 ± 0.006	1.882 ± 0.004	1.859 ± 0.003
c_3	0.69 ± 0.05	0.707 ± 0.008	0.707 ± 0.009
s_3	1 ± 0.2	1.00 ± 0.02	0.88 ± 0.07
a_o	$(2.2 \pm 0.4) \times 10^{-8}$	$(2.40 \pm 0.07) \times 10^{-4}$	$(1.0 \pm 0.2) \times 10^{-8}$
p	-3.44 ± 0.03	-3.26 ± 0.03	-3.62 ± 0.04
b_o	$(2.6 \pm 0.2) \times 10^{-3}$	$(1.00 \pm 0.06) \times 10^{-3}$	$(2.96 \pm 0.04 \times 10^{-3}$

Table S8: Fit parameters for HMT-PMBI(I^-), after soaking.

	97.5% dm	89.7% dm	80.2% dm
a_1	$(3.4 \pm 0.3) \times 10^{-4}$	$(3 \pm 2) \times 10^{-4}$	$(1.5 \pm 0.1) \times 10^{-4}$
b_1	0.379 ± 0.003	0.39 ± 0.02	0.365 ± 0.004
c_1	0.15 ± 0.01	0.3 ± 0.4	0.29 ± 0.02
s_1	1.0 ± 0.3	0 ± 0.3	0.0 ± 0.2
a_2	$(2.43 \pm 0.05) \times 10^{-3}$	$(1.3 \pm 0.1) \times 10^{-3}$	$(9 \pm 1) \times 10^{-4}$
b_2	1.215 ± 0.002	1.222 ± 0.005	1.17 ± 0.02
c_2	0.473 ± 0.007	0.53 ± 0.03	0.57 ± 0.04
s_2	1.00 ± 0.05	0.7 ± 0.2	0.66 ± 0.09
a_3	$(5.45 \pm .06) \times 10^{-3}$	$(2.9 \pm 0.2) \times 10^{-3}$	$(4.4 \pm 0.2) \times 10^{-4}$
b_3	1.827 ± 0.003	1.882 ± 0.009	1.76 ± 0.06
c_3	1.06 ± 0.02	1.05 ± 0.05	0.6 ± 0.1
s_3	0.04 ± 0.05	0.0 ± 0.2	1.00 ± 0.05
a_o	$(5.4 \pm 0.3) \times 10^{-7}$	$(3.4 \pm 0.5) \times 10^{-9}$	$(2.8 \pm 0.3) \times 10^{-9}$
p	-3.05 ± 0.01	-3.60 ± 0.03	-3.62 ± 0.02
b_o	$(1.39 \pm 0.05) \times 10^{-3}$	$(2.3 \pm 0.3) \times 10^{-3}$	$(1.71 \pm 0.01) \times 10^{-4}$

Table S9: Fit parameters for HMT-PMBI(Cl^-), after soaking.

	97.5% dm	89.7% dm	80.2% dm
a_1			$(1 \pm 1) \times 10^{-4}$
b_1			0.2 ± 0.1
c_1			4 ± 2
s_1			0.6 ± 0.4
a_2	$(2.72 \pm 0.08) \times 10^{-3}$	$(4.1 \pm 0.2) \times 10^{-3}$	$(2.58 \pm 0.07) \times 10^{-3}$
b_2	1.124 ± 0.003	1.127 ± 0.008	1.091 ± 0.002
c_2	0.509 ± 0.008	0.57 ± 0.01	0.70 ± 0.02
s_2	1.00 ± 0.08	1.00 ± 0.04	0.2 ± 0.1
a_3	$(8.2 \pm 0.1) \times 10^{-3}$	$(7.9 \pm 0.1) \times 10^{-3}$	$(3.0 \pm 0.1) \times 10^{-3}$
b_3	1.889 ± 0.002	1.878 ± 0.003	1.859 ± 0.004
c_3	0.78 ± 0.01	0.71 ± 0.03	0.78 ± 0.03
s_3	0 ± 0.08	0.6 ± 0.2	0.10 ± 0.09
a_o	$(8.2 \pm 0.9) \times 10^{-4}$	$(1.1 \pm 0.3) \times 10^{-5}$	$(4 \pm 2) \times 10^{-3}$
p	-0.82 ± 0.04	-1.82 ± 0.06	-3.66 ± 0.09
b_o	$(1.4 \pm 0.2) \times 10^{-3}$	0.0021 ± 0.0001	$(2.5 \pm 0.1) \times 10^{-3}$

Table S10: Length scales corresponding to each peak position, vacuum.

Sample	MAXS Peak (Å)	Peak 1 (Å)	Peak 2 (Å)
97.5% dm HMT-PMBI(I^-)	17.9 ± 0.1	$5.62 \pm .01$	$3.65 \pm .01$
89.7% dm HMT-PMBI(I^-)	18.0 ± 0.2	$5.73 \pm .01$	$3.74 \pm .02$
80.2% dm HMT-PMBI(I^-)	18.9 ± 0.2	$5.81 \pm .02$	$3.70 \pm .03$
65.9% dm HMT-PMBI(I^-)	20.2 ± 0.5	$6.05 \pm .02$	$3.91 \pm .02$
97.5% dm HMT-PMBI(Cl^-)	18.4 ± 0.1	$6.00 \pm .01$	$3.78 \pm .02$
89.7% dm HMT-PMBI(Cl^-)	19.9 ± 0.2	$6.37 \pm .01$	$3.80 \pm .02$
80.2% dm HMT-PMBI(Cl^-)	20.0 ± 0.2	$6.47 \pm .02$	$3.86 \pm .02$
65.9% dm HMT-PMBI(Cl^-)	21.9 ± 0.3	$6.51 \pm .02$	$3.93 \pm .02$

Table S11: Length scales corresponding to each peak position, ambient.

Sample	MAXS Peak (Å)	Peak 1 (Å)	Peak 2 (Å)
97.5% dm HMT-PMBI(I^-)	19 ± 2	$6.27 \pm .03$	$4.14 \pm .02$
89.7% dm HMT-PMBI(I^-)	$19.7 \pm .3$	$6.34 \pm .01$	$4.27 \pm .01$
80.2% dm HMT-PMBI(I^-)	$21.5 \pm .1$	$6.68 \pm .02$	$4.42 \pm .02$
97.5% dm HMT-PMBI(Cl^-)	22 ± 3	$6.59 \pm .03$	$4.08 \pm .01$
89.7% dm HMT-PMBI(Cl^-)	23 ± 2	$6.92 \pm .01$	$4.07 \pm .01$
80.2% dm HMT-PMBI(Cl^-)	23 ± 3	$7.16 \pm .01$	$4.12 \pm .01$

Table S12: Length scales corresponding to each peak position, soaked.

Sample	MAXS Peak (Å)	Peak 1 (Å)	Peak 2 (Å)
97.5% dm HMT-PMBI(I^-)	$20.2 \pm .2$	$6.31 \pm .01$	$4.20 \pm .01$
89.7% dm HMT-PMBI(I^-)	20 ± 1	$6.27 \pm .03$	$4.07 \pm .02$
80.2% dm HMT-PMBI(I^-)	$21.0 \pm .2$	$6.6 \pm .1$	$4.4 \pm .2$
97.5% dm HMT-PMBI(Cl^-)		$6.82 \pm .02$	$4.06 \pm .01$
89.7% dm HMT-PMBI(Cl^-)		$6.80 \pm .05$	$4.08 \pm .01$
80.2% dm HMT-PMBI(Cl^-)	40 ± 40	$7.03 \pm .01$	$4.12 \pm .01$